Particle Image Velocimetry Measurements of the Separation Bubble on an Iced Airfoil

Jason J. Jacobs[*] and Michael B. Bragg[†]

University of Illinois at Urbana-Champaign, Urbana, IL, 61801, USA

The separation bubble on a NACA 0012 airfoil with a two-dimensional, constant span, simulated leading-edge glaze-ice accretion is investigated using Particle Image Velocimetry (PIV). Chordwise PIV measurements, or those along the separation bubble cross-section, are obtained at a Reynolds number of 0.9×10^6, Mach number of 0.20, and between 0 deg and 5 deg angle-of-attack. Mean reattachment estimated from surface oil-flow visualization indicates increasing bubble length and unsteadiness (based on reattachment zone width) with angle-of-attack, consistent with results extracted from PIV measurements. Time-averaged streamlines and forward flow intermittency reveal a primary recirculation with clockwise rotation defined by a shear layer and a smaller, secondary recirculation with counter-clockwise rotation directly downstream of the point of separation, both consistent with backward-facing step type flowfields. Mean and RMS velocity component contours highlight these features and wall-normal profiles are extracted and compared to other separation bubble data including those over a backward-facing step and blunt flat plate.

I.   Introduction

ICE accretion on an airfoil surface changes the shape and thus the flowfield, pressure distribution, and aerodynamic performance of the airfoil. In general this means increased drag, reduced maximum lift and premature stall, variation in pitching moment, and overall reduction in control surface effectiveness. Due to these undesirable effects and their implications for flight safety, understanding the ice accretion process and the aerodynamic performance of iced airfoils is very important. The following describes this flowfield in detail and briefly summarizes select studies conducted to investigate it.

In many cases, ice accretion takes place on the airfoil leading edge creating a growth centered at the stagnation point with backward-facing step like geometries on both the pressure and suction surfaces. Bragg et al.[2] provides a description of the flowfield resulting from this type of leading-edge modification, a schematic of which is presented in Fig. 1. As Bragg describes, the laminar or transitional boundary layer separates off the suction surface horn due to a sufficiently strong adverse pressure gradient and a shear layer forms between this separated region and the inviscid flow above. Pressure recovery is delayed in this region resulting in a constant pressure plateau until the shear layer transitions to turbulent flow. At this point, vortex motion within the shear layer entrains higher velocity inviscid flow and mixes it with lower velocity flow in the separated region. At sufficiently low angle-of-attack, this mixing is enough to allow pressure recovery and the flow reattaches as a turbulent boundary layer. This reattachment is unsteady and defines a separation bubble whose size and shape vary in time. At larger angle-of-attack where the required pressure recovery cannot be achieved, reattachment occurs intermittently or not at all. This results in a bubble bursting phenomenon which initiates premature airfoil stall.
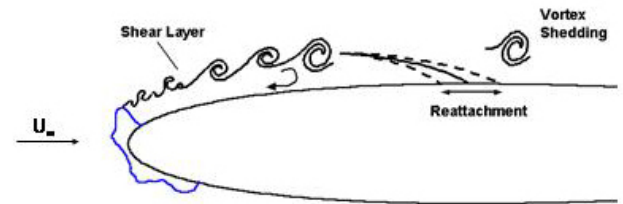

Fig. 1. Schematic of Separation Bubble on Airfoil With Leading-Edge Ice Accretion[1]

[*]Graduate Research Assistant, Department of Aerospace Engineering.

[†]Professor and Head, Department of Aerospace Engineering, Fellow AIAA.

Gurbacki and Bragg[1] and Gurbacki[3] conducted time-averaged and unsteady surface-pressure measurements, wake surveys, surface oil-flow visualization, and Particle Image Velocimetry (PIV) on a NACA 0012 with two- and three-dimensional simulated leading-edge glaze-ice accretions. In these studies, the cross-section of the two-dimensional ice simulation was the spanwise averaged cross-section of the three-dimensional shape. For both of the simulated accretions, the mean reattachment length, as well as the chordwise extent of the reattachment zone (unsteady bubble length variation), were shown to increase with angle-of-attack up to stall which was reduced some 10 deg by the accretions. Power spectra of time-dependent surface-pressure data near reattachment also revealed unsteadiness with nondimensional frequency $S_t = f x_{MR}/V_\infty = 0.53 - 0.73$ attributed to shear-layer vortices and vortex shedding from the separation bubble. Here f is the dimensional frequency, x_{MR} is the location of mean reattachment or bubble length, and V_∞ is the freestream velocity. Furthermore, broadband low-frequency unsteadiness was reported near stall with $S_t = 0.01$ based on time-dependent surface-pressure integrated lift coefficient power spectra. Because of its frequency, this unsteadiness was thought to be a vertical oscillation or flapping of the shear layer. Both unsteady modes are consistent with separation bubble unsteadiness reported in backward-facing step flows by Eaton and Johnston[4] and Driver et al.[5] and in blunt flat plate flows by Kiya and Sasaki[6,7] and Cherry et al.[8]

Gurbacki and Bragg[1] and Gurbacki[3] further compared the time-averaged and unsteady flowfields and performance of the constant span, two-dimensional smoothed ice accretion with that of the three-dimensional cast ice accretion. The most striking difference between the two was revealed in the flow visualization which showed a significant reduction in bubble length behind the three-dimensional ice accretion. Furthermore, this separation bubble was non-uniform in the spanwise direction, consisting of cells that did not correspond to noticeable features along the span of the three-dimensional ice accretion. These cells were attributed to a spanwise instability excited by the casting roughness which produced streamwise vortex structures that curved the streamlines within the separation bubble, particularly near the separation and reattachment lines. It was also proposed that these structures enhance mixing between the inviscid flow and separation bubble, aiding pressure recovery, shortening bubble length, and reducing the maximum lift coefficient and stall angle penalty relative to the two-dimensional ice accretion. A similar spanwise instability was observed in linear stability analyses of DNS solutions of backward-facing step flow by Barkley[9] and laminar separation bubble flow by Theofilis.[10,11]

As demonstrated by this brief review, much research has focused on separation bubbles from geometries such as the backward-facing step and blunt flat plate as well as clean airfoils and those with leading-edge ice accretions. Despite this attention, however, few detailed quantitative flowfield measurements have been taken to characterize the separation bubble, particularly related to the vortical flow structure which is closely related to shear-layer reattachment and boundary-layer development downstream. Therefore the objective of this investigation is to improve the understanding of the iced airfoil separation bubble and other unsteady, largely separated, reattaching flowfields and provide data useful in improving the computational methods used to predict them.

II.   Experimental Methods

Experiments were performed at the University of Illinois Aerodynamics Research Laboratory (ARL) in a 15-inch x 15-inch x 48-inch test section wind tunnel constructed specifically for this PIV investigation. The test section incorporates a glass sidewall and ceiling panel for laser and camera access and is preceded by an inlet contraction of area ratio 29:1 and a settling section containing a 4-inch thick honeycomb flow straightener and four stainless steel 24-mesh turbulence reducing screens. A 4 deg equivalent cone angle diffuser connects the test section to a 125 Hp, 16-bladed fan which may be exhausted into the tunnel room or through a 90 deg turning vane section vented outdoors, as is done when the flow is seeded for PIV.

The wind tunnel model is an 8-inch chord, 14.95-inch span, solid aluminum NACA 0012. The model mounts vertically in the test section and is supported by bolting the spar extending from the base of the model to the test section turntable which is used to manually adjust the model angle-of-attack to within ±60 seconds or 0.017 deg. Twenty static pressure taps are installed on a plane 5-inches from the base of the model, five on the pressure surface, one at the leading edge, and the remaining 14 along the suction surface. This coarse distribution, chosen to reduce model cost, is not sufficient for performance measurements, however it allows alignment of the clean model and provides limited information on separation bubble reattachment.

The two-dimensional ice shape used in these experiments is a geometrically-scaled model of that tested by Gurbacki and Bragg[1] and Gurbacki[3] in the ARL 3 foot x 4 foot wind tunnel. While Gurbacki evaluated sev-

eral ice shapes, she focused primarily on a 3.5 minute, 27.5°F glaze-ice accretion acquired in the BFGoodrich Icing Wind Tunnel at liquid water content (LWC) and mean volumetric diameter (MVD) conditions of 0.55 g/m^3 and 20 μm respectively. The accretion was formed on an 18-inch chord, 22-inch span NACA 0012 model at 4 deg angle-of-attack. A mold was taken of this accretion from which the three-dimensional casting tested by Gurbacki was produced using a polyurethane elastomer technique developed at the NASA Glenn Research Center.[12] An additional casting was produced, cut, and traced allowing an average cross-section to be defined using Surface Modelling and Grid Generation for Iced Airfoils (SmaggIce) software, also developed at the NASA Glenn Research Center. This cross-section was extruded and manufactured using stereolithography and served as the two-dimensional ice shape tested by Gurbacki. Furthermore, it is this geometry which has been scaled and manufactured, also using stereolithography, for PIV testing. Because the original three-dimensional casting cannot be geometrically-scaled, the three-dimensional ice shape used for PIV testing was created by adhering 20-grit roughness elements to the two-dimensional ice shape. This simulation technique was shown to most closely reproduce the flowfield behind the three-dimensional ice accretion in a series of surface oil-flow visualization experiments on both the 18-inch and 8-inch chord models.

PIV measurements were acquired with a LaVision FlowMaster 3S PIV system. As shown in Fig. 2, this system consists of a dual 120 mJ Gemini Nd:YAG PIV laser, a Kodak ES1.0 1 megapixel cross-correlation camera, and a dual 600 MHz processor acquisition computer running Microsoft Windows XP and LaVision's Data Acquisition and Visualization Software (DaVis) v6.2. Olive oil was used to seed the flow and was atomized using two TSI Model 9307 Laskin nozzle type oil droplet generators, producing 1.0 μm mean diameter particles, and two TSI Model 9306 six-jet atomizers, producing 0.6 μm mean diameter particles. All four seeders were connected to a 4-inch diameter PVC manifold with two rows of six 1/2-inch nozzles which was positioned in front of the tunnel settling section and oriented to uniformly seed the area of interest. This area was illuminated by a laser sheet which entered the

Fig. 2. LaVision FlowMaster 3S PIV System Setup

test section through the glass sidewall, oriented parallel to the tunnel floor, at a spanwise location determined by the height of the laser table. The camera imaged this area from above through a glass window set into the test section ceiling.
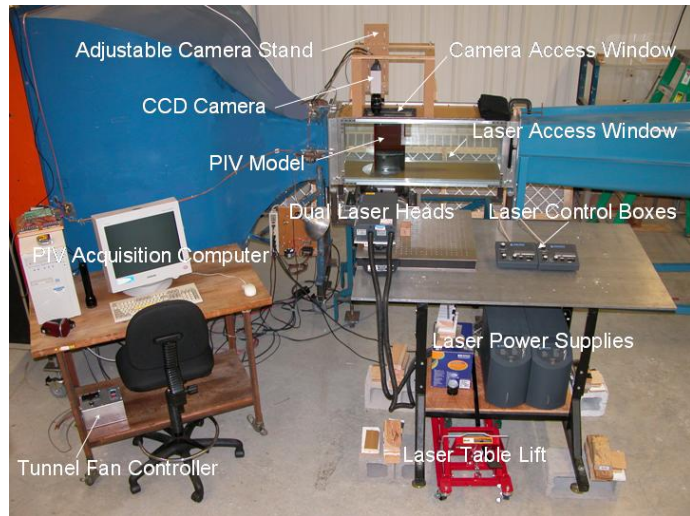
Experiments were performed at a Reynolds number of 0.9×10^6 and Mach number of 0.20. Steady model pressure distributions were acquired by a Pressure Systems Incorporated 8400 electronic scanning pressure (ESP) system between -5 deg and 6 deg angle-of-attack in one degree increments, the upper limit imposed to prevent saturation of the 1 psi ESP transducer module. All pressure taps, including those located in the settling section and test section inlet from which test section dynamic pressure and freestream velocity were derived, were sampled at 100 Hz for one second and time averaged.

Surface oil-flow visualization was performed to map the separation bubble length and reattachment zone versus angle-of-attack and to locate spanwise cell structures behind the three-dimensional ice simulation for future examination by PIV. A mineral oil and fluorescent dye mixture was sprayed on the model and the tunnel run for approximately 60 seconds during which time the mixture would flow over the model, driven by the local shear. The results were illuminated with ultra-violet lighting and photographed for later processing using a Nikon D100 digital SLR camera with a 35-105 mm Nikkor zoom lens with haze filter. This process was performed between 0 deg and 6 deg angle-of-attack in one degree increments.

PIV measurements were acquired between 0 deg and 5 deg angle-of-attack in one degree increments, the range over which separation bubble reattachment occurred on the suction surface. One thousand image pairs were acquired at each angle-of-attack at a rate of approximately 3 pairs per second, limited by the frame rate of the camera in cross-correlation mode and the speed and memory of the acquisition computer. A 60 mm Nikkor lens delivered a field-of-view of approximately 1.6-inches, or 19% chord. The correlation analysis,

American Institute of Aeronautics and Astronautics Paper 2006-3646

performed on a 2.6 GHz Windows machine using LaVision's DaVis v6.2, was a multi-pass adaptive algorithm with an interrogation cell size of 32 pixels square yielding a vector spacing of approximately 0.025-inches at 50% overlap. Vector validation was by a median filter routine which identified spurious vectors based on spatial RMS variation and replaced them with the average of neighboring vectors. All other processing occurred in MATLAB 6.0 using subroutines developed at Illinois.

III.   Results and Discussion

A.   Steady Pressure Distributions

Clean PIV model steady pressure distributions along with those with the two- and three-dimensional ice simulations were acquired and compared to data by Gurbacki. These measurements, along with surface oil-flow visualization comparisons presented in the next section, show that the flowfields generated on the 8-inch model for PIV investigation are consistent with those examined by Gurbacki and Bragg[1] and Gurbacki[3] on the 18-inch chord model. Results are presented for 4 deg angle-of-attack, however, the level of agreement shown is present across the full range of angle-of-attack examined with the tunnel exhausted both indoors and out.

Figure 3 shows steady pressure distributions on the 8-inch chord PIV model compared to those on the 18-inch chord model tested by Gurbacki, all at 4 deg angle-of-attack. The PIV model, identified as "8-inch", was run at 0.9×10^6 Reynolds number and 0.20 Mach number and the 18-inch chord model, at 1.8×10^6 Reynolds number and 0.18 Mach number. Clean pressure distributions are presented in Fig. 3(a) where the PIV model is virtually identical to the 18-inch chord model.

Pressure distributions with the two-dimensional ice shape are shown in Fig. 3(b). The ice shape ends at approximately 1% chord on the suction surface but the flow separation behind it results in a constant pressure region covering nearly the first 15% chord. At this point pressure recovery begins allowing reattachment farther downstream, approximately 29% chord on the PIV model at this angle-of-attack according to flow visualization. Reattachment on the 18-inch chord model appears to be even farther downstream as indicated by the more gradual pressure recovery and confirmed by flow visualization. This difference was first thought to be due to the increased freestream turbulence in the PIV tunnel relative to the 3 foot x 4 foot tunnel, a trend noted by Eaton and Johnston[13] in their review of turbulent reattachment research and by Kiya and Sasaki[6] in their blunt flat plate experiments. This could potentially hasten transition to turbulence of the shear layer resulting in earlier reattachment and shorter separation bubble length. However, comparing the pressure data on the PIV model from open return and exhausted tunnel configurations, where turbulence intensity at this speed increases from approximately 0.36% to 0.42% of the freestream or by 17%, shows no difference. Because of this fact and the previous clean airfoil agreement, this difference is now
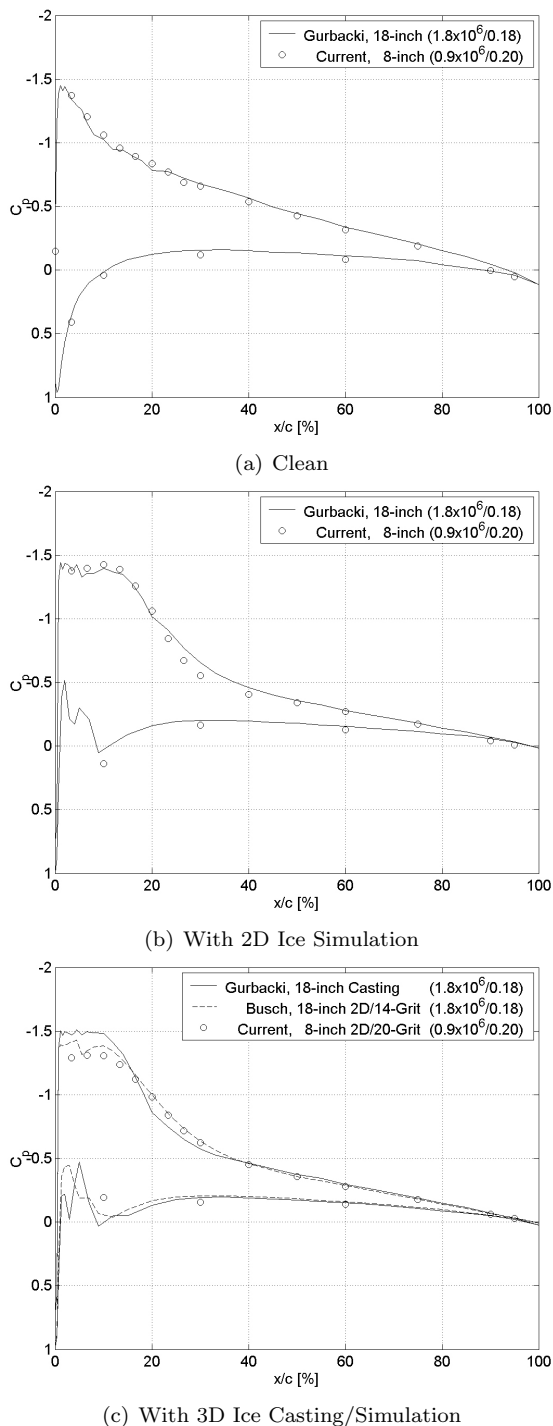

(a) Clean

(b) With 2D Ice Simulation

(c) With 3D Ice Casting/Simulation

Fig. 3.   Gurbacki[3] (18-inch) and Current (8-inch) Steady Pressure Distributions (α=4 deg)

thought to be related to the ice shape. Both 18-inch and 8-inch scale ice shapes were of stereolithography construction which typically delivers a surface tolerance of ±0.008-inches, however, this absolute tolerance represents a larger relative tolerance on the smaller ice shape. Furthermore, the 18-inch scale ice shape was bolted to the leading edge of the 18-inch chord model whereas the 8-inch scale ice shape was attached to the PIV model using RTV silicone, a method which relies on matching the interior contour of the ice shape with the model leading edge for alignment. The combination of these two factors is the most likely explanation for the difference seen in the two-dimensional iced pressure distributions in Fig. 3(b).

Finally, the three-dimensional ice casting and simulation pressure distributions are shown in Fig. 3(c). Also shown on this figure is a three-dimensional ice simulation by Busch[14] (dashed line) where 14-grit roughness was applied to the two-dimensional ice shape on the 18-inch chord model to simulate the spanwise variation of the three-dimensional casting. This simulation does not reach the same low pressure plateau achieved by the casting and has a more gradual recovery. Likewise, the 20-grit based three-dimensional ice simulation tested on the PIV model recovers more gradually from a lower pressure peak than the casting but matches closely the simulation by Busch. These results indicate that the roughened two-dimensional ice shape does not exactly match the actual three-dimensional ice casting in terms of pressure distribution, however, it is reasonably close. Furthermore, flow visualization in the next section will demonstrate the similarity in behavior versus angle-of-attack between the casting and simulation and in the flow structure including spanwise cells generated inside the separation bubble. Finally, it should be noted that comparing flow visualization on the 18-inch chord model with the three-dimensional ice casting and the PIV model with the three-dimensional ice simulation shows the casting to have a longer separation bubble even though it appears in Fig. 3(c) to recover more quickly than the simulation, the opposite trend as seen in Fig. 3(b) with the two-dimensional ice shape. This is possibly due to the fact that the casting and simulation are not simply different geometric scales of the same geometry but undoubtedly indicates that reattachment cannot be accurately gleaned strictly from the pressure distribution.

B. Surface Oil-Flow Visualization

Flow visualization was also performed on the PIV model and compared to images of the 18-inch chord model taken by Gurbacki to further validate the sub-scale flowfields generated on the PIV model.

(a) 18-inch 2D ($1.8 \times 10^6/0.18$)

(b) 18-inch 3D ($1.8 \times 10^6/0.18$)

(c) 8-inch 2D ($0.9 \times 10^6/0.20$)

(d) 8-inch 3D ($0.9 \times 10^6/0.20$)

Fig. 4. Gurbacki[3] (18-inch) and Current (8-inch) Surface Oil-Flow Visualization (Flow Left to Right, α=4 deg)

Figure 4 shows these images at 4 deg angle-of-attack. The box around each of the 18-inch chord images represents the full span of the model and illustrates both models are of equal aspect ratio. Figures 4(a) and 4(c) are with the two-dimensional ice shape and Figs. 4(b) and 4(d), the three-dimensional ice casting and 20-grit roughness based ice simulation, respectively. In all cases, flow is from left to right and the ice shape is visible on the left side of the image. Finally the tape applied along the chord in each image indicates
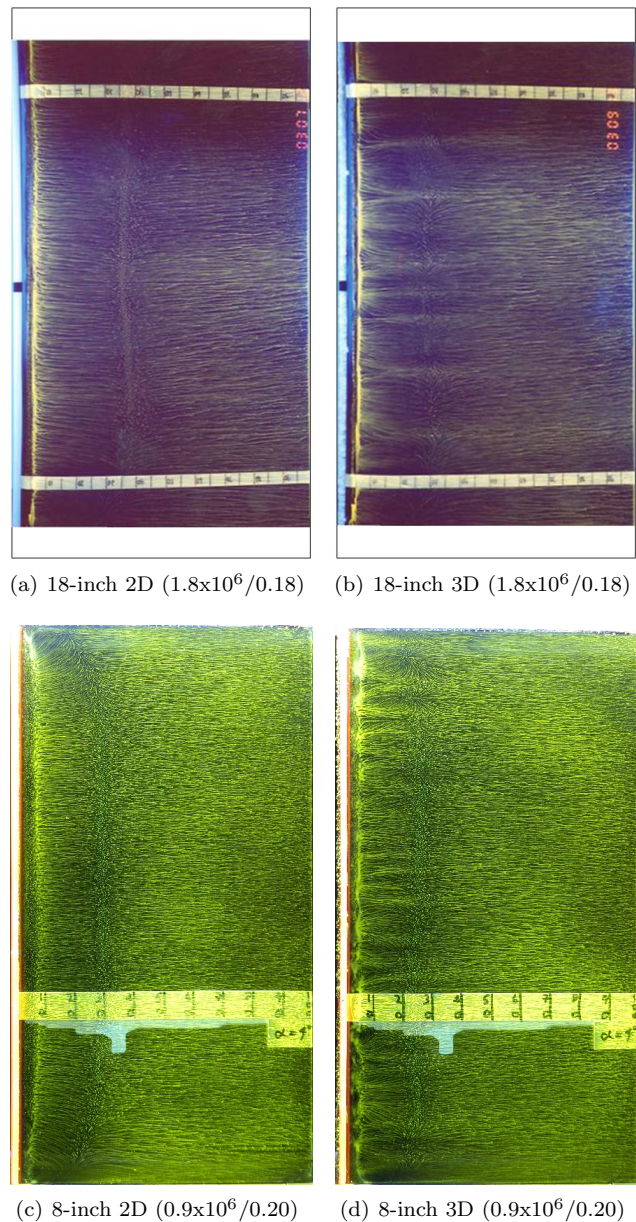
percent chord, x/c, from 0% to 100% and is used to locate important flow features such as reattachment.

As discussed in Section I and illustrated in Fig. 1, the flow separates from the horn on the upper surface of the ice shape generating a shear layer separating a low velocity, recirculating separation bubble from the inviscid flow above. Vortices in this shear layer entrain higher energy flow into the separation bubble initiating pressure recovery at sufficiently low angle-of-attack. This results in flow reattachment farther downstream, an unsteady process which in the mean appears as a thin, vertical, speckled region as seen between 35% and 40% chord in Fig. 4(a). The center of this region is considered mean reattachment. Upstream of this location inside the separation bubble, the flow is low velocity and near the model surface, primarily in the reverse streamwise direction. Downstream, the flow has reattached as a turbulent boundary layer and moves toward the trailing edge.

Again referring to Fig. 4, first note the approximately 5% chord shorter bubble on the PIV model than the 18-inch chord model with both the two- and three-dimensional ice shapes. This was noted in Fig. 3(b) where the PIV model appeared to recover from its low pressure peak more quickly than the 18-inch chord model, both with the two-dimensional ice shape. This would not be expected based on Fig. 3(c), however, as it is the 18-inch chord model with three-dimensional ice casting which appears to recover more quickly. But as noted in the previous section, the pressure distribution cannot be relied upon exclusively for locating mean reattachment. Second, note the spanwise variation within each separation bubble in Fig. 4. Behind the two-dimensional ice shape and away from the test section floor and ceiling, the mean reattachment line is straight and the streamlines inside the separation bubble are parallel to the freestream. Behind the three-dimensional ice casting and simulation, however, the streamlines inside the separation bubble are curved indicating the presence of a spanwise velocity component, w. This is the instability discussed in previous sections whose origin will be investigated in detail through future spanwise PIV measurements.

Figure 5 summarizes the mean reattachment on the above models versus angle-of-attack up to 5 deg. First note for each model, the shear layer reattaches some 5-10% farther upstream behind the three-dimensional ice shape than the two-dimensional. Gurbacki[3] suggests this is due to the same vortex structures which generate three-dimensional flow inside the separation bubble behind the casting. She says these vortices possibly aid in the entrainment of higher energy flow into the separation bubble, further promoting pressure recovery and shortening bubble length. While this has been reported in the literature, such as by Westphal and Johnston[15] who noted shortened reattachment lengths downstream of a backward-facing step when small triangular vortex generators were placed upstream of the separation point, a thorough PIV investigation of these vortex structures, including their relationship to separation bubble length, is currently underway. Also note in Fig. 5 how the difference in separation bubble length between the PIV and 18-inch chord models increases with angle-of-attack from approximately 2% chord at 0 deg to 10% chord or more at 5 deg. As discussed previously, this difference is thought to be the result of tolerances and positioning of the 8-inch scale ice shape on the PIV model. A sensitivity study by Blumenthal et al.[16] used the Gurbacki model to
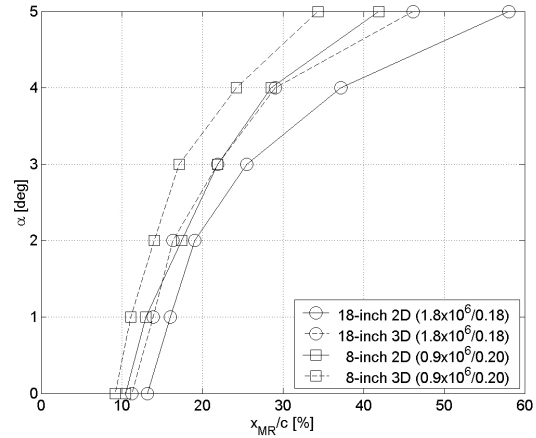

Fig. 5. Gurbacki[3] (18-inch) and Current (8-inch) Mean Reattachment From Flow Visualization
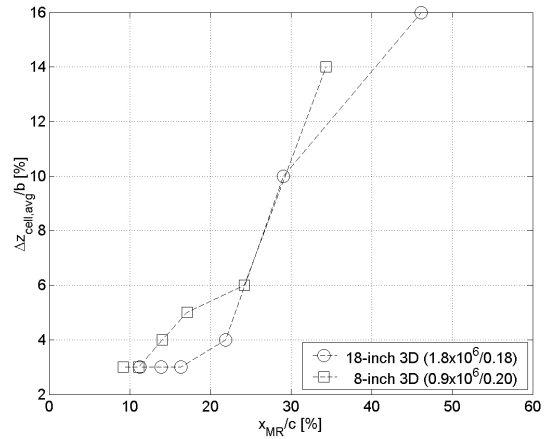

Fig. 6. Average Spanwise Cell Spacing Behind Gurbacki[3] 3D Ice Casting (18-inch) and Current 3D Ice Simulation (8-inch) From Flow Visualization

examine the effect of horn height and radius of the same two-dimensional ice shape studied here on airfoil performance and separation bubble length. These results suggest a 0.015-inch (7%) change in horn height on the 8-inch scale ice shape could shift reattachment on the PIV model by 5% chord. While this deviation is nearly twice the SLA profile tolerance, superimposing the effect of horn height, radius, and angle tolerances could likely explain the difference in reattachment length summarized in Fig. 5.

One last comparison of flow visualization results involves the average spanwise cell spacing behind the three-dimensional ice casting and simulation. It has been observed that this spacing is related to separation bubble length and this hypothesis is consistent with the flow visualization images in Figs. 4(b) and 4(d). Shown at the same angle-of-attack, the shorter separation bubble on the 8-inch chord model consists of a larger number of more closely spaced spanwise cells than the longer separation bubble on the 18-inch chord model. This notion can also be found in the literature. Barkley[9] performed linear stability analyses on backward-facing step DNS solutions and found the critical eigenmode to be a spanwise periodic structure similar to the spanwise cells observed in Fig. 4. By studying the instability mechanism, he argued the instability is centrifugal in nature according to Rayleigh's criterion[17] in which recirculating flow, such as that inside the separation bubble, in some cases can give rise to out-of-plane secondary flow. Because it is the eddies inside this recirculating region which drive the instability, it is the length of this region which is the appropriate length scale for the instability. This is supported in Fig. 6 where the average spanwise cell spacing in percent span is plotted versus mean reattachment length in percent chord for both the 18-inch chord model with the three-dimensional ice casting and the 8-inch chord PIV model with the three-dimensional ice simulation. This relationship, derived from examining flow visualization images, is approximately linear and shows spanwise cells growing larger and fewer in number with increasing separation bubble length. Also note both models collapse on this plot further supporting the applicability of the roughness-based three-dimensional ice simulation for this investigation.

C.   Particle Image Velocimetry

This investigation involves PIV measurements along multiple chordwise and spanwise planes of the 8-inch chord PIV model with both the two- and three-dimensional ice simulations. To date, however, only chordwise PIV measurements with the two-dimensional ice simulation have been both acquired and processed. Therefore, this section will focus only on these results while the three-dimensional data and comparisons between the ice simulations will be presented in future publications.

Figure 7 shows an image of the seeded flow at 0 deg angle-of-attack. The model is visible at the bottom of the image and the ice shape, at the bottom left. The separation bubble runs from the back of the ice shape until reattachment near 12% chord. The shear layer is clearly visible extending from the tip of the ice shape horn and separating the bubble from the inviscid flow above. Vortices are also seen inside the shear layer as small regions of low seed concentration where the flow rotation has centrifuged the higher-than-air-density olive oil particles away from the vortex core. Vortices are also visible downstream of reattachment supporting previous findings of separation bubble vortex shedding such as by Kiya and Sasaki.[6]

A PIV correlation analysis was performed on the image shown in Fig. 7 along with its image pair using LaVision's DaVis v6.2 resulting in a single instantaneous velocity vector field. After all image pairs were correlated, further calculations proceeded in MATLAB including that of the mean velocity vector field shown in Fig. 8. The velocity vectors are shaded by magnitude between zero velocity and 40% higher than the 216 ft/s freestream velocity. Superimposed onto the velocity field are two representative separation bubble streamlines as defined by Khodadoust.[18] The lower is the stagnation streamline and represents the height above the model where the time-averaged streamwise velocity component, $\overline{u}$, is zero. This streamline divides the reverse flow in the lower region of the separation bubble from the forward flow above. The upper streamline is the separation or dividing streamline and represents the height above the model, y_{sep}, where the integrated streamwise mass-flow below is zero and for incompressible flow is given by:

$$\int_{y_{surf}/c}^{y_{sep}/c} \frac{\overline{u}}{V_\infty}\, d\left(\frac{y}{c}\right) = 0\,. \tag{1}$$

This streamline perhaps better illustrates the mean bubble as it extends above the stagnation streamline until there is zero net streamwise mass-flow below, just as there would be if the mean separation bubble was replaced by a solid wall.
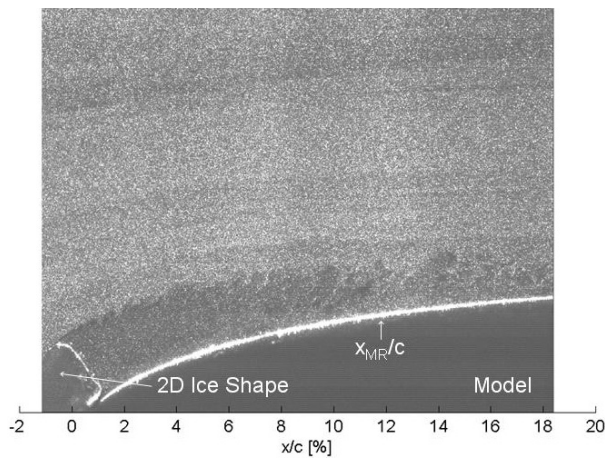
Fig. 7. Olive Oil Seeded Flow Over PIV Model With 2D Ice Shape (Flow Left to Right, α=0 deg)
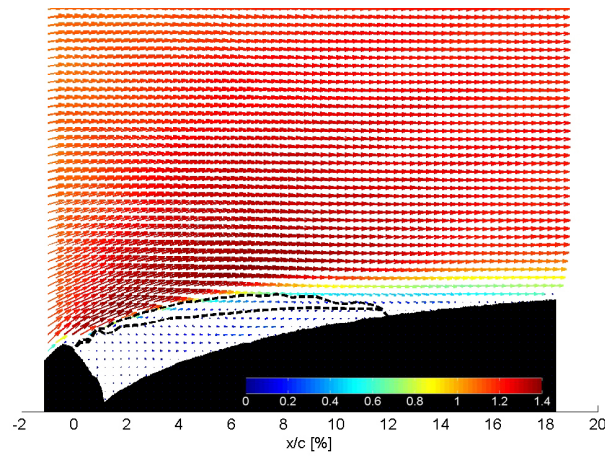

Fig. 8.   Mean Velocity Vector Field, $\overline{\vec{V}}/V_\infty$ [R_e= 0.9x10^6, M_∞=0.20, α=0 deg, $--$ Sep.(Upper) and Stag.(Lower) Streamlines]
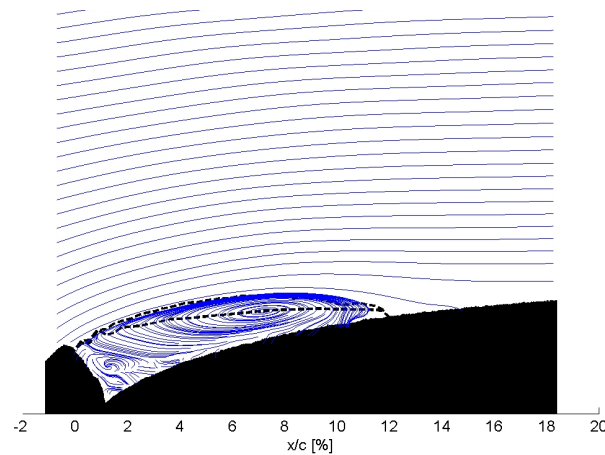

Fig. 9.   Mean Streamlines [R_e=0.9x10^6, M_∞=0.20, α=0 deg, $--$ Sep.(Upper) and Stag.(Lower) Streamlines]
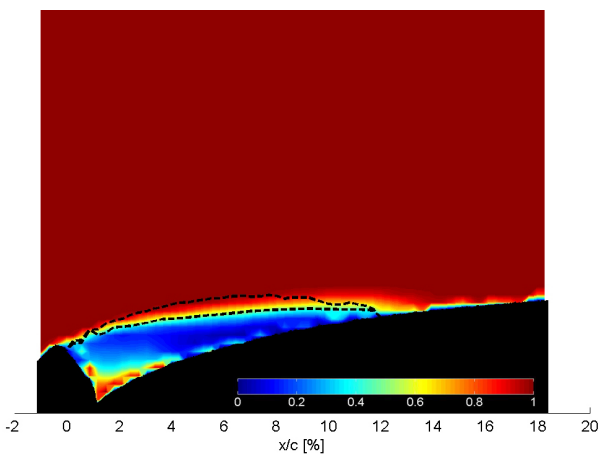

Fig. 10.   Forward Flow Intermittency [R_e=0.9x10^6, M_∞= 0.20, α=0 deg, $--$ Sep.(Upper) and Stag. (Lower) Streamlines]

Figure 9 shows streamlines integrated from the mean velocity field shown in Fig. 8. Note the primary (clockwise) recirculation inside the separation bubble with the stagnation streamline coinciding with the locus of points with zero mean streamwise velocity. And just above, separating the recirculating region from the inviscid flow is the separation streamline. Also note both streamlines intersect the model at approximately 12% chord, very near the mean reattachment location as determined from flow visualization. A smaller secondary recirculation with counter-clockwise rotation is also visible directly downstream of the ice shape, extending to approximately 3% chord at 0 deg angle-of-attack. This structure grows with increasing angle-of-attack, as does the primary recirculation, and both are characteristic of backward-facing step type flows such as those investigated by Kostas et al.[19] and Hudy et al.[20]

Both the primary and secondary recirculations can also be seen in the forward flow intermittency shown in Fig. 10. Intermittency represents the percentage of vector field realizations with positive streamwise velocity. Thus zero intermittency at a given point indicates the streamwise flow at that location is zero or negative in each of the vector fields acquired whereas an intermittency of unity indicates the streamwise flow is in the downstream direction in each vector field. Inside the separation bubble and below the stagnation streamline, the mean flow is almost entirely reversed and the intermittency is very low except directly downstream of the ice shape inside the secondary recirculation. Here the counter-clockwise rotation results in high intermittency near the wall. Above the stagnation streamline, the recirculating flow is moving downstream
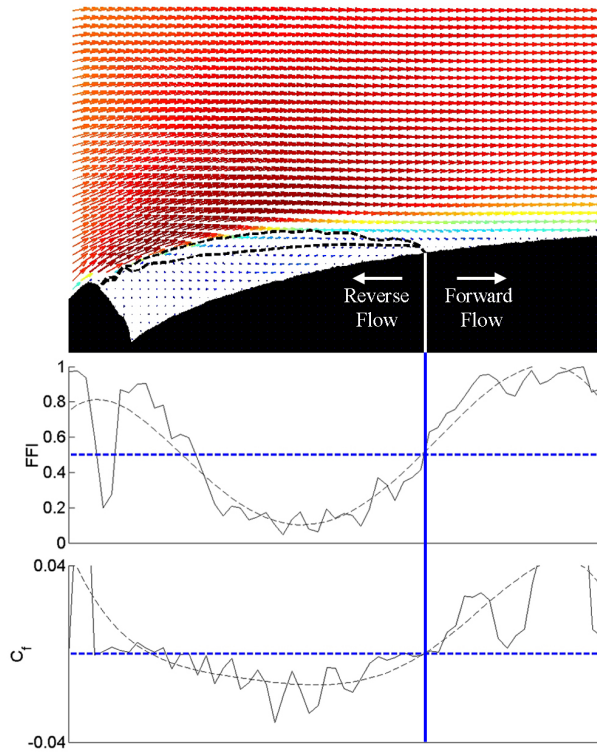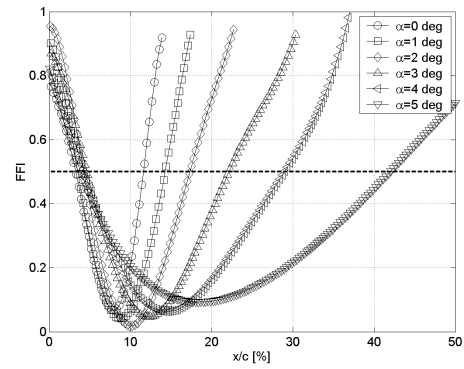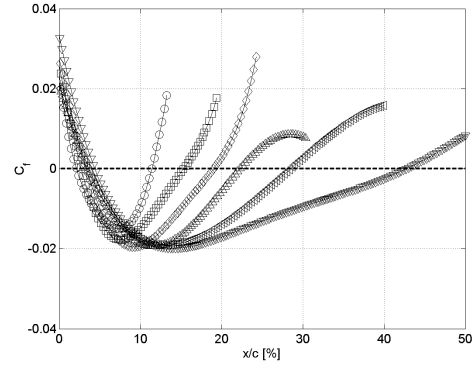
Fig. 11. Schematic of Mean Reattachment Estimation From PIV Mean Velocity Field

(a) Forward Flow Intermittency

(b) Skin Friction

Fig. 12. Chordwise Distribution of Intermittency and Skin Friction for Estimation of Mean Reattachment (R_e=0.9x10^6, M_∞=0.20)

and the intermittency increases reaching unity above the shear layer.

As shown in Fig. 10, intermittency also increases from near zero to unity across the location of mean reattachment, making it a convenient locator of this point. An intermittency of 0.50 near the wall, meaning one-half of the vector realizations at that point have positive streamwise velocity, is considered mean reattachment. A second method used for estimating mean reattachment from PIV data is based on the chordwise distribution of skin friction. At a given chordwise location, the mean streamwise velocity profile is differentiated with respect to the wall-normal coordinate, η, at or near the wall and skin friction is calculated directly as:

$$C_f = \frac{\tau_w}{1/2 \, \rho_\infty u_e^2} \tag{2}$$

where u_e is the boundary-layer edge-velocity and τ_w, the wall-shear stress:

$$\tau_w = \mu \left. \frac{\partial \overline{u}}{\partial \eta} \right|_{\eta \approx 0} . \tag{3}$$

In this case, the separation bubble is characterized by negative skin friction indicating reverse flow near the wall and the location of zero skin friction is considered mean reattachment. Both methods of estimating mean reattachment are illustrated in Fig. 11 as the location of 0.50 intermittency aligns with the location of zero skin friction and the intersection of the stagnation and separation streamlines with the wall. Note the solid lines in Fig. 11 are raw data and the dashed lines, 5th-order polynomial fits.

Polynomial fits of intermittency and skin friction chordwise distributions are presented in Fig. 12 for the PIV model with the two-dimensional ice simulation between 0 deg and 5 deg angle-of-attack. Both methods agree closely and are averaged to provide an estimate of mean reattachment according to PIV. These results are then compared to flow visualization reattachment data in Fig. 13. To verify that the flowfield behind
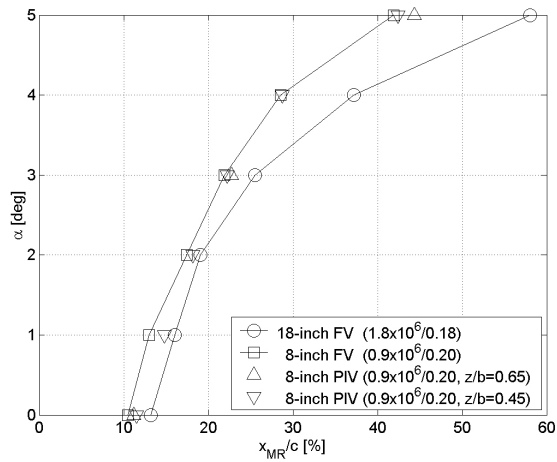
Fig. 13. Comparison of Mean Reattachment on Gur-backi[3] (18-inch) and Current (8-inch) Models From PIV and Flow Visualization (2D Ice Shape)

Fig. 14. Mean Streamwise Velocity, $\overline{u}/V_\infty$ [R_e= 0.9x10^{6}, M_∞=0.20, α=0 deg, $--$ Sep.(Upper) and Stag.(Lower) Streamlines]

the two-dimensional ice shape is indeed two-dimensional, PIV data were acquired on two chordwise planes, z/b=0.45 ($\bigtriangledown$) and limited angles-of-attack at z/b=0.65 ($\triangle$). The largest deviation in mean reattachment according to PIV between the two chordwise planes is less than 2% chord and occurs at 5 deg angle-of-attack. Furthermore, mean reattachment according to PIV along both chordwise planes deviates from flow visualization results by less than 2% chord between 0 deg and 5 deg angle-of-attack.

Flowfield statistics are now presented in the form of filled contour plots and wall-normal profiles and compared to existing backward-facing step type flow measurements. Mean and RMS streamwise velocity, both normalized by the freestream velocity, are shown in Figs. 14 and 15, respectively. The large velocity gradient across the shear layer is visible in Fig. 14 as well as the low-velocity flow inside the separation bubble. The contour levels in this plot range from zero to 1.3. The shear layer can be seen even more clearly in Fig. 15 as the region with large RMS streamwise velocity fluctuations, shown from zero to 0.35. Note how thin the shear layer is between the point of separation and approximately 5% chord before expanding rapidly toward the wall to a thickness approaching the effective height of the ice shape, or that of the downstream face of the ice shape normal to the airfoil. Also note how the separation streamline bisects the shear layer, running through the region of maximum RMS streamwise velocity from the point of separation until just upstream of reattachment. This is consistent with the identification of the shear-layer center by Kiya and Sasaki[6] as the locus of maximum RMS streamwise velocity. Furthermore, along this locus, two local RMS streamwise velocity peaks can be identified, the first and larger being just downstream of separation in the
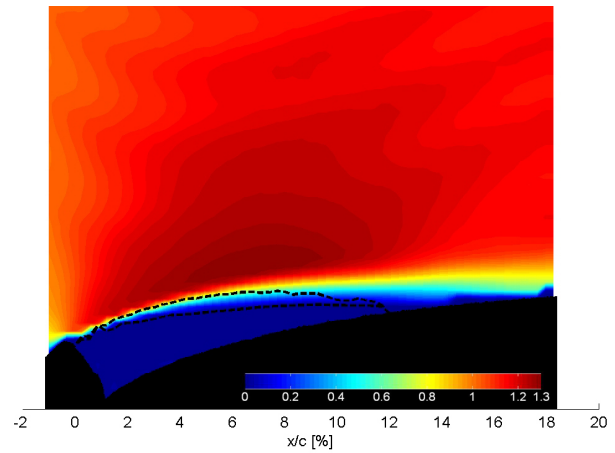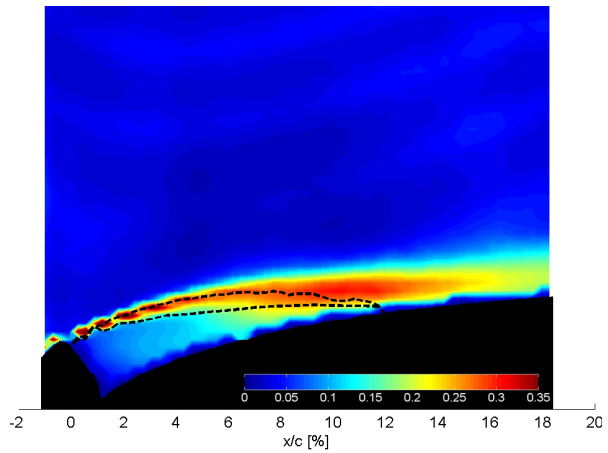

Fig. 15. RMS Streamwise Velocity, u_{RMS}/V_∞ [R_e= 0.9x10^{6}, M_∞=0.20, α=0 deg, $--$ Sep.(Upper) and Stag.(Lower) Streamlines]
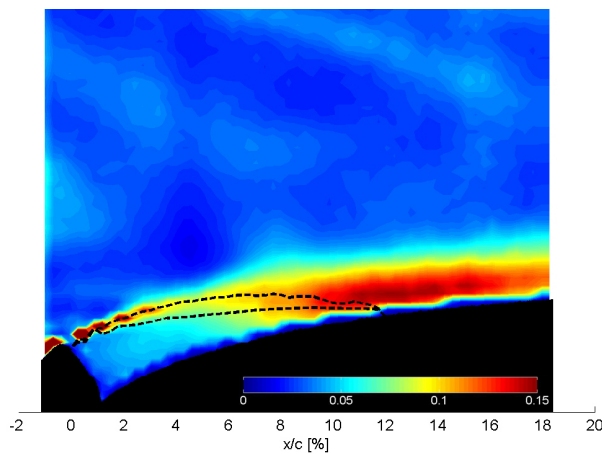

Fig. 16. RMS Normal Velocity, v_{RMS}/V_∞ [R_e= 0.9x10^{6}, M_∞=0.20, α=0 deg, $--$ Sep.(Upper) and Stag. (Lower) Streamlines]

thin region of the shear layer and the second, just upstream of mean reattachment. Finally, downstream of mean reattachment, RMS streamwise velocity decays quickly as the shear layer reattaches as a turbulent boundary layer. This qualitative picture of the RMS streamwise velocity field is very similar to backward-facing step flows examined by both Kostas et al.[19] and Hudy et al.[20] It also parallels time-dependent surface pressure measurements by Gurbacki and Bragg[1] and Gurbacki[3] who noted peak RMS surface pressure just upstream of mean reattachment behind both the two- and three-dimensional ice simulations reproduced for this investigation.

RMS normal velocity is presented in Fig. 16 with contour levels ranging from zero to 0.15. As with RMS streamwise velocity, the RMS normal velocity field has two distinct peaks, the first and larger near the point of separation, and the second near mean reattachment. The latter, however, is farther downstream and broader than in the case of RMS streamwise velocity with a value near 0.14 running from 10% chord to 15% chord. As a result, with respect to peak RMS velocities near mean reattachment, fluctuations in the normal direction persist farther downstream than those in the streamwise direction.

Surface-normal profiles of mean streamwise velocity and RMS streamwise and normal velocity are presented for 0 deg angle-of-attack in Figs. 17-19 at three chordwise locations, 10.19% chord, 11.84% chord (mean reattachment from PIV), and 14.31% chord. The chordwise locations upstream and downstream of mean reattachment correspond to backward-facing step (BFS) PIV profiles presented by Hudy et al.[20] which are reproduced here ($\boxminus$) for comparison to the iced airfoil separation bubble profiles from this study ($\ominus$). That is in each case, the length along the airfoil surface between the separation point and the profile normalized by the separation bubble surface length is the same for each geometry, approximately 0.85 for the upstream profile and 1.22 for the downstream profile. In terms of effective step height, the airfoil profiles are located at ξ/h of 3.94, 4.58, and 5.53 where ξ is the surface length from the intersection of the ice shape and model and the backward-facing step profiles are located at x/h=4.23 and 6.07. Backward-facing step reattachment profiles at x/h=4.97 were not available, however, split-film measurements by Kiya and Sasaki[6] at mean reattachment on a blunt flat plate (BFP), x/h=10.1, are presented ($\diamond$) and compared to the iced airfoil reattachment profiles. The backward-facing step data were acquired at a Reynolds number based on step height of 32,327, the closest available to the airfoil data whose 0.9×10^6 chordwise Reynolds number corresponds to approximately 24,000 Reynolds number based on the upper surface horn height normal to the airfoil. Blunt flat plate data were acquired at 26,000 Reynolds number based on the plate half-thickness, h. All profiles are normalized by the boundary-layer edge-velocity to account for the airfoil streamwise pressure gradient and the profiles are plotted versus the surface-normal coordinate, η, normalized by the 99% edge-velocity boundary-layer thickness, δ.

First note in Fig. 17 the streamwise reverse flow inside the iced airfoil separation bubble upstream of mean reattachment and at mean reattachment, the near zero derivative of streamwise velocity with respect to the wall-normal coordinate indicating zero shear stress. Finally downstream of mean reattachment, the streamwise velocity assumes an attached profile. Similar trends are observed in both the backward-facing step and blunt flat plate profiles.

RMS streamwise velocity profiles are presented in Fig. 18 at the same locations as the mean profiles in Fig. 17. Peak RMS streamwise velocity near mean reattachment on the iced airfoil was approximately 0.24. This is considerably higher than the maximum RMS streamwise velocity measured by Hudy et al.[20] on the backward-facing step, approximately 0.18. It also exceeds the maxima summarized by Eaton and Johnston[13] in their review of subsonic turbulent flow reattachment, approximately 0.10 to 0.21 based on hot-wire measurements on single- and double-sided sudden expansions with Reynolds numbers based on step height ranging from 11,000 to 60,000. This value is nearly identical, however, to the maximum RMS streamwise velocity measured by Kiya and Sasaki[6] on the blunt flat plate, 0.24. It also compares well to laser Doppler velocimetry (LDV) measurements by Khodadoust[18] on a NACA 0012 with a similar simulated leading-edge glaze-ice accretion at a chordwise Reynolds number of 1.5×10^6, or 53,000 based on the ice shape effective height. The maximum RMS streamwise velocity measured by Khodadoust[18] was 0.22, also normalized by the boundary-layer edge-velocity, and occurred just upstream of mean reattachment. Based on the freestream velocity, the maximum RMS streamwise velocities from the blunt flat plate, the current iced airfoil, and that investigated by Khodadoust[18] were approximately 0.25, 0.30 and 0.34, respectively. Finally, also note in Fig. 18 the location of the shear-layer center with respect to the boundary-layer thickness, indicated by the location of the RMS streamwise velocity peak. The backward-facing step profiles indicate the shear layer was centered near η/δ =0.25 at x/x_{MR}=0.85 and 1.22 whereas the iced airfoil shear-layer center moved from approximately η/δ=0.50 to 0.25 over the same distance. This can also be seen in the mean streamwise velocity
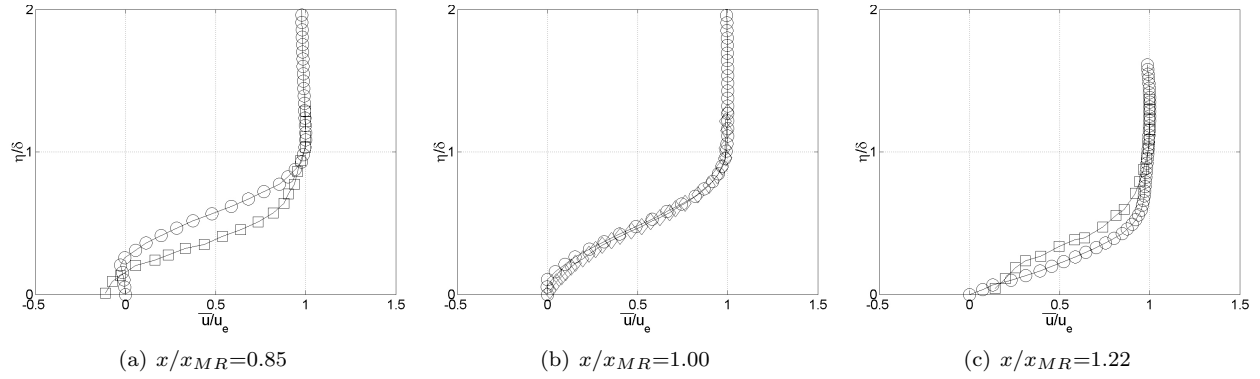
(a) x/x_{MR}=0.85   (b) x/x_{MR}=1.00   (c) x/x_{MR}=1.22

Fig. 17. Mean Streamwise Velocity, $\overline{u}/u_e$, ⊕ Current (R_{e_h}=24,000), ⊟ Hudy et al.[20] (BFS PIV, R_{e_h}=32,327), ◇ Kiya and Sasaki[6] (BFP Split-Film, R_{e_h}=26,000)

(a) x/x_{MR}=0.85   (b) x/x_{MR}=1.00   (c) x/x_{MR}=1.22
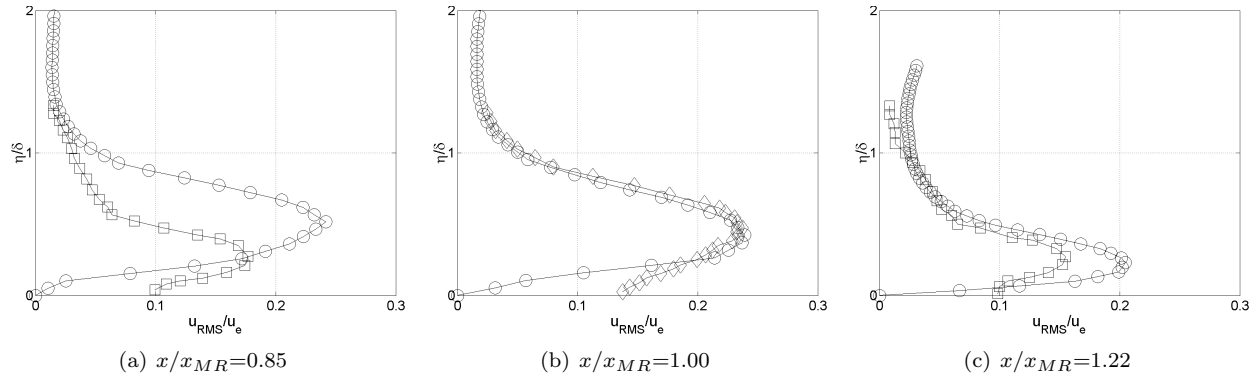
Fig. 18. RMS Streamwise Velocity, u_{RMS}/u_e, ⊕ Current (R_{e_h}=24,000), ⊟ Hudy et al.[20] (BFS PIV, R_{e_h}=32,327), ◇ Kiya and Sasaki[6] (BFP Split-Film, R_{e_h}=26,000)

(a) x/x_{MR}=0.85   (b) x/x_{MR}=1.00   (c) x/x_{MR}=1.22
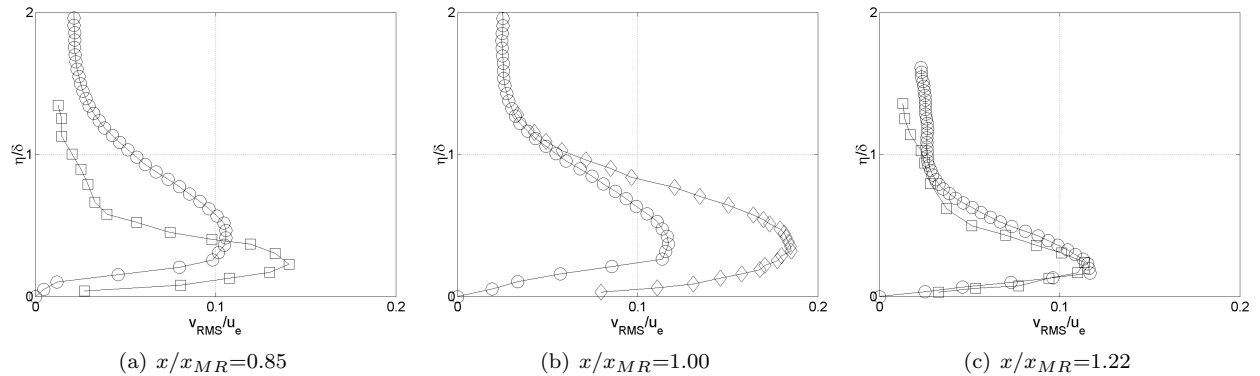
Fig. 19. RMS Normal Velocity, v_{RMS}/u_e, ⊕ Current (R_{e_h}=24,000), ⊟ Hudy et al.[20] (BFS PIV, R_{e_h}=32,327), ◇ Kiya and Sasaki[6] (BFP Split-Film, R_{e_h}=26,000)

profiles in Fig. 17 by approximating the shear-layer center as the center of the region of large streamwise velocity gradient with respect to the wall-normal coordinate. Blunt flat plate profiles at corresponding locations upstream and downstream of mean reattachment were not available, however, it is clear that the boundary-layer thickness increased along the flat plate such that the shear layer tended toward the wall as seen in the iced airfoil profiles. Thus, increased maximum RMS streamwise velocity and trajectory of the shear-layer center across mean reattachment possibly differentiate the iced airfoil and blunt flat plate flows from that of the backward-facing step, however, more thorough comparisons of the flowfield statistics will be required to understand these relationships.

RMS normal velocity profiles are presented in Fig. 19 where the peak values upstream of mean reattachment for the iced airfoil and backward-facing step were approximately 0.11 and 0.14, respectively. And as

with the RMS streamwise velocity, the iced airfoil peak occurred nearly twice the distance from the wall, in terms of the boundary-layer thickness, as did the backward-facing step peak. Downstream of reattachment, the iced airfoil RMS normal velocity peak likewise shifted toward the wall, however, its magnitude remained relatively constant as the backward-facing step peak decayed to approximately 0.11. At mean reattachment, the iced airfoil and blunt flat plate RMS normal velocity peaks aligned with magnitudes approximately 0.12 and 0.19 respectively.

IV.   Conclusions

The primary objective of this research was to understand the similarities and differences between the flowfield structure of the separation bubbles formed on a NACA 0012 airfoil with simulated leading-edge two- and three-dimensional glaze-ice accretions. A new 15-inch x 15-inch test section wind tunnel has been assembled for PIV experiments to investigate these flowfields. An appropriate aspect ratio model and three-dimensional ice simulation have been identified which generate sub-scale flowfields consistent with those examined by Gurbacki and Bragg[1] and Gurbacki[3] and hardware has been fabricated. Time-averaged pressure distributions and surface oil-flow visualization on this new hardware confirmed that these flowfields are indeed consistent with the full-scale flowfields of interest in terms of mean reattachment behavior with angle-of-attack and spanwise cell structure and spacing.

Chordwise PIV images of the seeded flow over the model with the two-dimensional ice simulation showed small vortex structures inside the shear layer emanating from the suction surface horn and larger vortex activity downstream. A large clockwise recirculating region enclosed by the shear layer and small counter-clockwise recirculating region centered at the interface of the ice shape and model were also visible and grew with increasing angle-of-attack. The mean location of shear-layer reattachment, determined from the chordwise distribution of forward flow intermittency and skin friction, was very near the location of mean reattachment according to surface oil-flow visualization. This location also corresponded to the intersection of the model and the bubble stagnation and separation streamlines, the later of which connected the locus of points with maximum RMS streamwise velocity defining the center of the shear layer.

Wall-normal mean streamwise velocity profiles were interpolated indicating reverse flow near the model surface inside the separation bubble, zero gradient or skin friction at mean reattachment, and an attached profile downstream. These results were consistent with backward-facing step PIV profiles acquired by Hudy et al.[20] and blunt flat plate split-film measurements acquired by Kiya and Sasaki.[6] Maximum RMS streamwise velocity near mean reattachment was approximately 0.24 normalized by the boundary-layer edge-velocity. This value was considerably higher than the maximum RMS streamwise velocity of 0.18 recorded by Hudy et al.[20] It was much closer, however, to the maximum RMS streamwise velocity measured by Kiya and Sasaki,[6] 0.24, and by Khodadoust,[18] 0.22, who acquired LDV data on a NACA 0012 with a similar leading-edge ice accretion. Also, the location of the maximum RMS streamwise velocity above the wall, which defines the shear-layer center, was shown to be relatively constant across mean reattachment in the backward-facing step profiles but shifted toward the wall in both the iced airfoil and blunt flat plate profiles. These similarities in both the value and trajectory of the peak RMS streamwise velocity between the iced airfoil and blunt flat plate suggest a relationship which will be examined by more thorough comparisons of the flowfield statistics.

Finally, the trajectories of peak RMS normal velocity were shown to be similar to those of the peak RMS streamwise velocity. The magnitude of the iced airfoil normal fluctuations, however, remained relatively constant several percent chord downstream of mean reattachment while the backward-facing step fluctuations decayed as in the streamwise direction. The maximum RMS normal velocities near mean reattachment for the iced airfoil, backward-facing step, and blunt flat plate were approximately 0.12, 0.14, and 0.19, respectively.

V.   Acknowledgment

American Institute of Aeronautics and Astronautics Paper 2006-3646

References

[1] Gurbacki, H. M. and Bragg, M. B., "Unsteady Aerodynamic Measurements on an Iced Airfoil," *AIAA Paper 2002-0241*, 40th AIAA Aerospace Sciences Meeting & Exhibit, Reno, NV, January 2002.

[2] Bragg, M. B., Khodadoust, A., and Spring, S. A., "Measurements in a Leading-Edge Separation Bubble due to a Simulated Airfoil Ice Accretion," *AIAA Journal*, Vol. 30, No. 6, 1992, pp. 1462–1467.

[3] Gurbacki, H. M., *Ice-Induced Unsteady Flowfield Effects On Airfoil Performance*, Ph.D. thesis, University of Illinois at Urbana-Champaign, Urbana, IL, 2003.

[4] Eaton, J. K. and Johnston, J. P., "Low frequency unsteadiness of a reattaching turbulent shear layer," *Turbulent Shear Flows III*, Third International Symposium on Turbulent Shear Flows, University of California at Davis, September 1981, pp. 162–170.

[5] Driver, D. M., Seegmiller, H. L., and Marvin, J. G., "Time-Dependent Behavior of a Reattaching Shear Layer," *AIAA Journal*, Vol. 25, No. 7, 1987, pp. 914–919.

[6] Kiya, M. and Sasaki, K., "Structure of a turbulent separation bubble," *Journal of Fluid Mechanics*, Vol. 137, 1983, pp. 83–113.

[7] Kiya, M. and Sasaki, K., "Structure of large-scale vortices and unsteady reverse flow in the reattaching zone of a turbulent separation bubble," *Journal of Fluid Mechanics*, Vol. 154, 1985, pp. 463–491.

[8] Cherry, N. J., Hillier, R., and Latour, M. E. M. P., "Unsteady measurements in a separated and reattaching flow," *Journal of Fluid Mechanics*, Vol. 144, 1984, pp. 13–46.

[9] Barkley, D., Gomes, M. G. M., and Henderson, R. D., "Three-Dimensional instability in flow over a backward-facing step," *Journal of Fluid Mechanics*, Vol. 473, 2002, pp. 167–190.

[10] Theofilis, V., Hein, S., and Dallmann, U., "On the origins of unsteadiness and three-dimensionality in a laminar separation bubble," *The Philosophical Transactions of the Royal Society of London, Series A*, Vol. 358, 2000, pp. 3229–3246.

[11] Theofilis, V., "On the spatial structure of global linear instabilities and their experimental identification," *Aerospace Science and Technology*, Vol. 4, 2000, pp. 249–262.

[12] Reehorst, A. L. and Richter, G. P., "New Methods and Materials for Molding and Casting Ice Formations," *NASA TM 100126*, September 1987.

[13] Eaton, J. K. and Johnston, J. P., "A Review of Research on Subsonic Turbulent Flow Reattachment," *AIAA Journal*, Vol. 19, No. 9, 1981, pp. 1093–1100.

[14] Busch, G., private communication, University of Illinois at Urbana-Champaign, Urbana, IL, July 2005.

[15] Westphal, R. V. and Johnston, J. P., "Effect of Initial Conditions on Turbulent Reattachment Downstream of a Backward-Facing Step," *AIAA Journal*, Vol. 22, No. 12, 1984, pp. 1727–1732.

[16] Blumenthal, L., Busch, G., Broeren, A. P., and Bragg, M. B., "Issues in Ice Accretion Aerodynamic Simulation on a Subscale Model," *AIAA Paper 2006-262*, 44th AIAA Aerospace Sciences Meeting & Exhibit, Reno, NV, January 2006.

[17] Bayly, B. J., "Three-Dimensional centrifugal-type instabilities in inviscid two-dimensional flows," *Physics of Fluids*, Vol. 31, 1988, pp. 56–64.

[18] Khodadoust, A., *An Experimental Study Of The Flowfield On A Semispan Rectangular Wing With Simulated Glaze Ice Accretion*, Ph.D. thesis, University of Illinois at Urbana-Champaign, Urbana, IL, 1993.

[19] Kostas, J., Soria, J., and Chong, M. S., "Particle image velocimetry measurements of a backward-facing step flow," *Experiments in Fluids*, Vol. 33, 2002, pp. 838–853.

[20] Hudy, L. M., Naguib, A. M., Humphreys, W. M., and Bartram, S. M., "Particle Image Velocimetry Measurements of a Two/Three-dimensional Separating/Reattaching Boundary Layer Downstream of an Axisymmetric Backward-facing Step," *AIAA Paper 2005-0114*, 43th AIAA Aerospace Sciences Meeting & Exhibit, Reno, NV, January 2005.